

Resonant magnetic induction tomography of a magnetized sphere

A. Gloppe,^{1,*} R. Hisatomi,¹ Y. Nakata,¹ Y. Nakamura,^{1,2} and K. Usami¹

¹*Research Center for Advanced Science and Technology (RCAST),
The University of Tokyo, Meguro-ku, Tokyo 153-8904, Japan*

²*Center for Emergent Matter Science (CEMS), RIKEN, Wako, Saitama 351-0198, Japan*

(Dated: December 15, 2024)

Collective spin excitations in solids can serve as an interface between quantum systems [1], coherently coupled to phonons [2], microwave and optical photons [3, 4]. Bulk dielectric magnetized solids of revolution, saturated along their symmetry axis, are the scenery of interactions between transverse spin-wave modes [5–8] and confined optical photon modes [9–14]. Advanced *in situ* insights on the spin-wave modes are required to push forward the understanding and control of these hybrid systems. However, owing to their geometry, the spatial mapping of the spin-wave modes in these structures has never been realized. Here, we demonstrate the structural imaging of spin-wave modes hosted in a magnetized solid of revolution by resonant magnetic induction tomography. Exemplified on a millimetric ferrimagnetic sphere, this method ensures the robust identification of the spin-waves modes, opening magnon hybrid systems to novel magnetic materials. We establish their azimuthal dependence, crucial for the advent of magnonic chiral photonics [15].

Macroscopic magnetically ordered structures, such as Yttrium Iron Garnet (YIG) millimetric spheres, are solid supports of extended collective spin excitations, *magnons*, that can be cooled down to their quantum ground state and coherently coupled to a superconducting quantum bit through a microwave cavity [3]. A coherent optical control of magnons in the quantum regime could enable the efficient transduction of optical and microwave photons [4], opening the way to quantum telecommunications between superconducting quantum computers [1] as well as quantum-noise limited microwave amplifiers [16]. The study of the interactions of magnons and photons in an optical cavity, or *cavity optomagnonics*, in a solid-state matrix has begun with the first observations of non-reciprocal magnon-induced Brillouin light scattering involving the uniform precession spin-wave mode and optical whispering gallery modes of a YIG sphere [9–11]. Higher-order magnetostatic spin-wave modes, with a variety of orbital angular momenta and spin textures, extend the richness of this hybrid system. In particular, the exchange of orbital angular momentum between magnons and optical photons has been experimentally demonstrated recently [14]. The optomagnonic coupling, faint with the uniform precession

mode, will be optimized for high-order modes whose spatial distribution localizes more and more towards the resonator boundaries where the optical whispering gallery modes spread [13].

These spin-wave modes can be described within the magnetostatic approximation for a saturated magnetic ellipsoid [5] and their eigenfrequencies determined numerically. Diverse effects could alter this description: related to the environment as the temperature dependence of the saturation magnetization, the non-uniformity of the saturating static magnetic field or the presence of close-by parasitic elements [8, 17], or related to the sample as propagation corrections [18], magneto-crystalline anisotropy [19] or irregularities and composition defects, potentially resulting in inter-mode coupling [20]. Increasing the optomagnonic coupling by using hybrid custom shapes with smaller mode volumes [12] will disturb the frequency distribution [6]. Associated with the density of modes excited by a non-uniform microwave field, the simple identification of the modes beyond the uniform precession mode using their expected ferromagnetic resonance frequencies [18] is possibly ambiguous. An *in situ* structural mapping of the spin-wave modes is needed to properly identify them and estimate their coupling to others modes, independently of the sample nature and of the experimental conditions, whether for fundamental magnonic studies [21] or for hybrid system operations [13, 14, 22, 23].

Pushed forward by the demands for fast recording and high-capacity storage devices, magnetization dynamics of micro and nanostructures on a substrate have been intensively studied in the last years with advanced magnetic microscopy methods involving x-ray magnetic circular dichroism [24], magneto-optical interactions [25], thermal effects [26], microwave near-field [27] and magnetic scanning probe [28]. At the other extreme, space exploration and geophysics have been implementing successfully magnetic field measurements around gigantic solids of revolution from satellite-based loop coil magnetometers employed to understand terrestrial polar aurorae from the ionosphere [29] to vector fluxgate magnetometers used to determine the magnetosphere and interior structures of Jupiter [30].

Here, we access the spatial structure of the spin-wave modes of a bulk magnetized solid by measuring the magnetic flux spectrum intercepted by a mobile loop coil facing the sample at different azimuth-altitude positions,

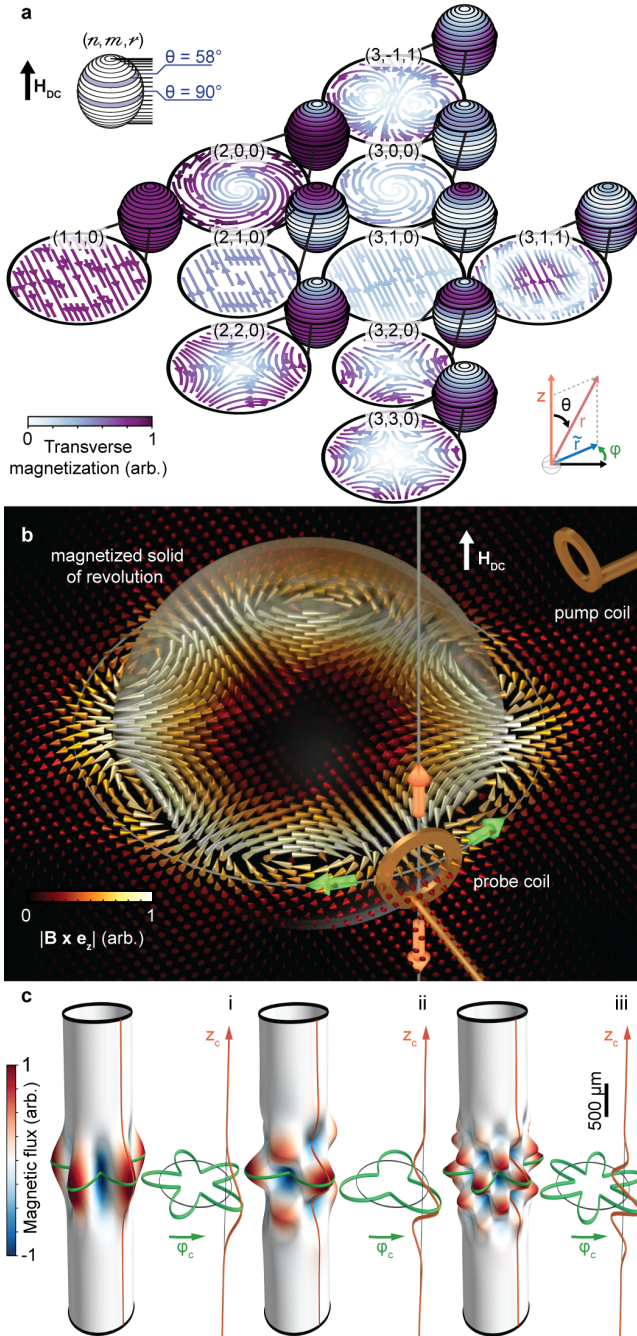


FIG. 1. Imaging the stray field induced by the spin-wave modes of a magnetized sphere. **a**, Snapshot of the calculated spatial magnetization distribution of magnetostatic modes in a YIG sphere for $n < 4$, transverse to the static magnetic field H_{DC} . Their magnetization norm is color-encoded for successive sections from $\theta = 10^\circ$ to 170° (see Methods). **b**, Schematic of the experiment. A fixed loop coil (pump coil) excites the magnons at microwave frequencies. These modes generate a dynamic magnetic field, represented here in the equatorial plane for the $(n, m, r) = (3, 3, 0)$ mode. The stray field spectrum is captured by a second loop coil (probe coil) at different azimuthal-altitude (φ_c, z_c) positions. **c**, Numerical calculations of the spatially-resolved magnetic flux intercepted by a rectangular coil ($\Delta_y = 0.5$ mm, $\Delta_z = 0.3$ mm, $\tilde{r}_c = 2$ mm) on a YIG sphere for $(n, m) = (5, 5)$, $(7, 3)$ and $(12, 6)$ families (i-iii), encoded in the surface colors and corrugations.

while the magnons are coherently excited by a fixed microwave antenna — realizing a magnetic resonance imaging (MRI) [31] scanner for collective electron spins excitations. The spatially and spectrally resolved magnetic responses of the system are carefully processed to extricate the nature of each spin-wave mode.

A strong magnetic field H_{DC} applied along the z -axis saturates the magnetization of the sample. Solving Maxwell and Landau-Lifshitz equations reveals the existence of dynamic magnetization modes in the orthogonal plane [6]. For a millimetric YIG sphere, these spin-wave modes have typical eigenfrequency $\Omega_k/2\pi \sim 5\text{--}10$ GHz for H_{DC} in the 100 mT/ μ_0 range (with μ_0 the magnetic constant). In the magnetostatic approximation [7], they are described by three indices (n, m, r) : m expresses the azimuthal dependency and is linked to the winding number of the spin texture [14], $n - |m|$ the polar dependency and r the number of nodes along the radial direction. Their spatial distribution is deduced from a magnetic potential solution of Laplace equation in oblate spheroidal coordinates dependent on the applied static magnetic field and on the considered mode. The non-trivial spatial distributions of the lowest-order modes are pictured in Fig. 1a, their phase dependence at fixed altitude being given approximately by $-(m-1)\varphi$. Outside the sphere, a magnetostatic mode induces a magnetic field $\mathbf{H}_n^m = \nabla\psi_n^m$ such that close to the magnon resonance

$$\psi_n^m(r, \theta, \varphi) = \frac{\zeta_n^m}{r^{n+1}} P_n^m(\cos \theta) e^{im\varphi}$$

with ζ_n^m encapsulating the pump field projection on the spin-wave mode and the resonance condition, while P_n^m is the Ferrers function [32]. The spherical coordinate system (r, θ, φ) is depicted in the inset of Fig. 1a. Figure 1b illustrates the imaging scheme. The pump coil, fixed during the experiment, applies a microwave field exciting the magnons. This antenna could be designed to maximize the pumping efficiency of spatially non-uniform spin-wave modes of interest. The excitation frequency is swept to measure the spectral response of the whole magnonic system. The probe coil turns around the sample axis of revolution along a cylindrical orbit (φ_c, z_c) and intercepts at each position the phase-resolved spectrum of the induced magnetic flux. Working at a cylindrical detection distance \tilde{r}_c large compared to the typical width $2\Delta_y$ and height $2\Delta_z$ of the probe coil, the induced flux due to a (n, m) mode can be approximated to $\phi_n^m(\varphi_c, z_c) \sim e^{im\varphi_c} \mathcal{Z}_n^m(z_c)$ with $\mathcal{Z}_n^m(z_c)$ having a mode-dependent envelope whose number of nodes along the altitude axis is related to $n - |m|$ [32]. Figure 1c presents numerical computations of the magnetic flux induced by some representative mode families. Rotating the probe coil around the sample at fixed altitude grants access to the azimuthal parameter m , enclosed in the mode relative phase, while a walk along the altitude z -axis leads to

the polar parameter $n - |m|$. The radial dependency, not affecting the spatial distribution of the stray field, has to be deduced from the suite of eigenfrequencies of a given family (n, m) [6]. Each excited mode, with its distinct spectral signature, will contribute to the total stray field. The extraction of these features in the measured spectra at all positions along these two axes leads to their spatial mapping and subsequently to their robust identification.

The studied sample is a 2 mm-diameter YIG sphere, placed at the center of an iron magnetic circuit ended by two permanent ring magnets distanced by 15 mm. The static magnetic field (~ 230 mT/ μ_0) created along their revolution axis z saturates the sphere along its [110] crystal axis. The two small loop coils with a sub-millimetric inner radius ($\Delta_y \sim 0.5$ mm, $\Delta_z \sim 0.3$ mm), made out of semi-rigid coaxial copper cables by terminating their ends, are facing the sample and are respectively connected to the output (pump) and input (probe) ports of a vector network analyzer. The fixed pump coil stands a few millimeters away from the sample. Fixed to a three-axis linear actuator on a motorized rotation stage, the probe coil takes arbitrary positions ($\tilde{r}_c, \varphi_c, z_c$) along a cylindrical orbit around the sample. The detection distance is set at $\tilde{r}_c = 2$ mm. The reflected power from the pump coil (Fig. 2a) reveals a collection of absorption dips, signatures of individual resonant spin-wave modes which can be modeled as damped harmonic oscillators [33]. We measure in transmission (Fig. 2b-c) the magnetic flux intercepted by the probe coil at a particular position $S_\phi[\Omega] = \sum_{k=\{n,m,r\}} A_k e^{i\varphi_k}/(\Omega - \Omega_k + i\Gamma_k \Omega)$ with k running on all the excited modes, $\Omega_k/2\pi$ the spin-wave mode eigenfrequency, Γ_k its damping rate, and A_k its relative response amplitude depending on the mode-dependent pump efficiency and on the mode spatial structure. The relative mode phase with respect to the excitation field, $\varphi_k = \varphi_k^0 + \varphi_k$, can be decomposed such that φ_k^0 is the mode phase origin defined by the excitation field and φ_k its spatial component.

For imaging the spatial structure of the spin-wave modes, we assemble these spectral measurements at numerous probe coordinates (φ_c, z_c) and adjust the local spin-wave mode responses. First at fixed altitude, the coil travels around the sample. Figure 3a depicts the transmitted ferromagnetic resonance signal power and phase spectra along the azimuth in the equatorial plane ($z_c = 0$). While the modes amplitude is globally constant, their relative phase φ_k individually changes with the probe azimuth. We report the evolution of the relative phase as a function of the coil azimuthal position. Figure 3b(i-vi) illustrates the extracted azimuthal dependence of the phase of six different modes, with their theoretical counterparts appended, insuring a clear identification of modes with $m = 0, 1, 2, 3, 4$ and 7 .

Next, at fixed azimuth we record the spectra along the altitude axis (Figure 4a). As we are traveling over

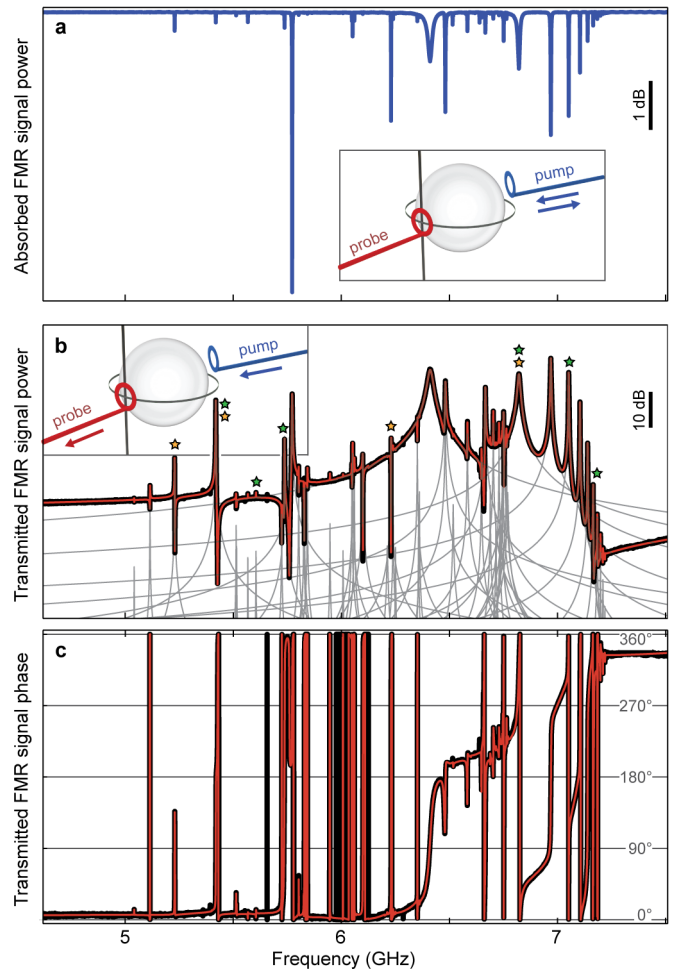


FIG. 2. Broadband ferromagnetic resonances (FMR) at a fixed azimuth-altitude coordinate. **a**, Typical spectrum of the microwave power reflected by a 2-mm YIG sphere into the pump coil (blue line). The absorption dips correspond to the resonance of more than 50 different individual spin-wave modes (resolution bandwidth: 10 kHz). The excitation microwave frequency range is chosen such that the spectrum encapsulates all the excited modes in one run. At a fixed probe-coil azimuth-altitude coordinate (φ_c, z_c) , the transmitted microwave spectra in power (b) and phase (c) (black line) intercepted by the probe coil through the sphere give access to the local information on each mode once fitted as a collection (red line) of individual harmonic oscillators (grey lines), in particular the local phase with respect to the origin fixed by the excitation field. All the measurements are repeated after an automatized vertical retraction of the sample to define robust phase references [32]. Colored stars mark the modes analyzed along the azimuth in Fig. 3 (green) and along the altitude in Fig. 4 (orange).

the mode envelope, the variation of the mode transmitted power and phase flips are observable directly on the spectra for well-isolated dominant modes. We report the extracted signed mode amplitude $A_k \cos \varphi_k$ as a function of the altitude of four representative modes in Fig. 4b(i-iv), illustrating polar mode families $n - |m| = 0, n - |m| = 1$,

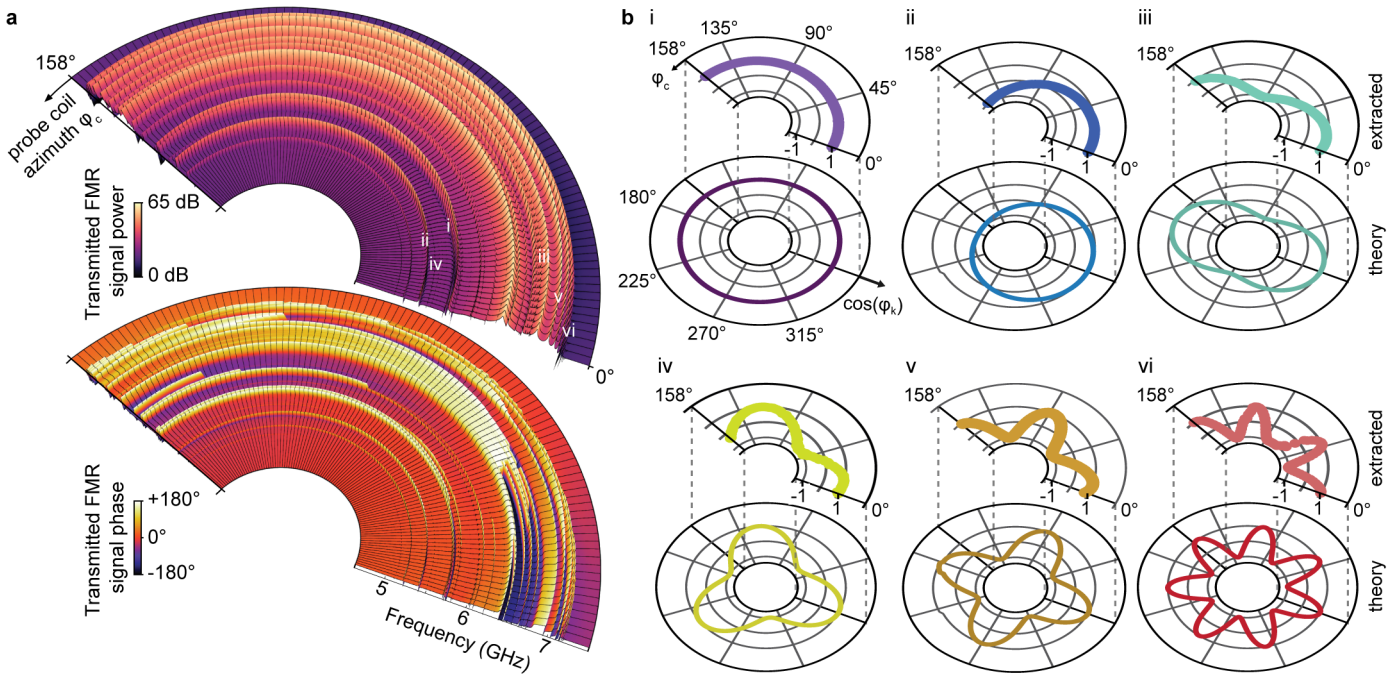


FIG. 3. **Azimuthal dependence of the induced magnetic flux.** **a**, Microwave transmission spectra in power and phase as a function of the azimuthal position of the probe coil φ_c in the sample equatorial plane. These spectra are all processed (see Figure 2 and Supplementary Information) to extract the relative phase of each spin-wave modes φ_k , exemplified by six of them in **b(i-vi)** (colored filled circles, top), with mean eigenfrequencies of 5.74 GHz, 5.42 GHz, 6.82 GHz, 5.61 GHz, 7.05 GHz and 7.17 GHz (indicated on **a** and on Fig. 2b with green stars), exhibiting an azimuthal parameter $m = 0, 1, 2, 3, 4$ and 7 respectively, in comparison with the theoretical evolution of $m\varphi_c$ (solid color lines, bottom).

$n - |m| = 2$ and $n - |m| = 3$. The altitude axis of the coil is slightly tilted by $\xi_z = -6^\circ$ with respect to the z -axis defined by the permanent magnets [32]. This induces a slight imbalance in the measured flux, favoring positive altitudes. The measurements are in very good agreement with the theoretical calculation of the flux taking into account this correction. The exhibited modes could be identified respectively as $(2, 2, 0)$, $(3, 2, 0)$, $(3, 1, 0)$ and $(4, 1, 0)$. Their relative eigenfrequencies spacing to the uniform precession mode $(\Omega_k - \Omega_{110})/2\pi$ are computed in the magnetostatic approximation for comparison [32]. The discrepancies with the experimental observations, respectively 15 %, -36 %, -8% and -8 %, most likely due to magneto-crystalline anisotropy and propagation effects, underline the necessity to access the mode spatial properties to avoid a misidentification between close-by modes. With a simple excitation field, our method reveals the polar mode families up to $n - |m| = 3$ and azimuthal families up to $m = 7$.

We have developed a broadband resonant tomography scanning method to map the spatial structure of spin-wave modes hosted in a magnetized solid of revolution, independent of the exact knowledge on the sample and on the experimental conditions. Demonstrated here on a 2-mm YIG sphere saturated along its [110] axis, this approach should be straightforwardly extended

to any custom combination shape of ellipsoids, disks or rods, as well as any magnetized samples exhibiting spin-wave modes with linewidths smaller than their typical frequency splitting. This versatile method will be particularly relevant for studying the magnetization dynamics of emergent magnetic materials and structures whose shape, crystallinity and composition could be challenging to control. Proper hybrid magnonic operations well beyond the uniform precession mode could be envisioned, broadening the scope of magnomechanics and cavity optomagnonics towards the emergence of an efficient interface based on macroscopic quantum systems.

Acknowledgments

The authors thank A. Osada, R. Yamazaki and Y. Tabuchi for fruitful interactions. This work was supported by JSPS KAKENHI (Grant Nos. 16F16364 and 26220601) and by JST ERATO project (Grant No. JP-MJER1601). A.G. is an Overseas researcher under Postdoctoral Fellowship of Japan Society for the Promotion of Science.

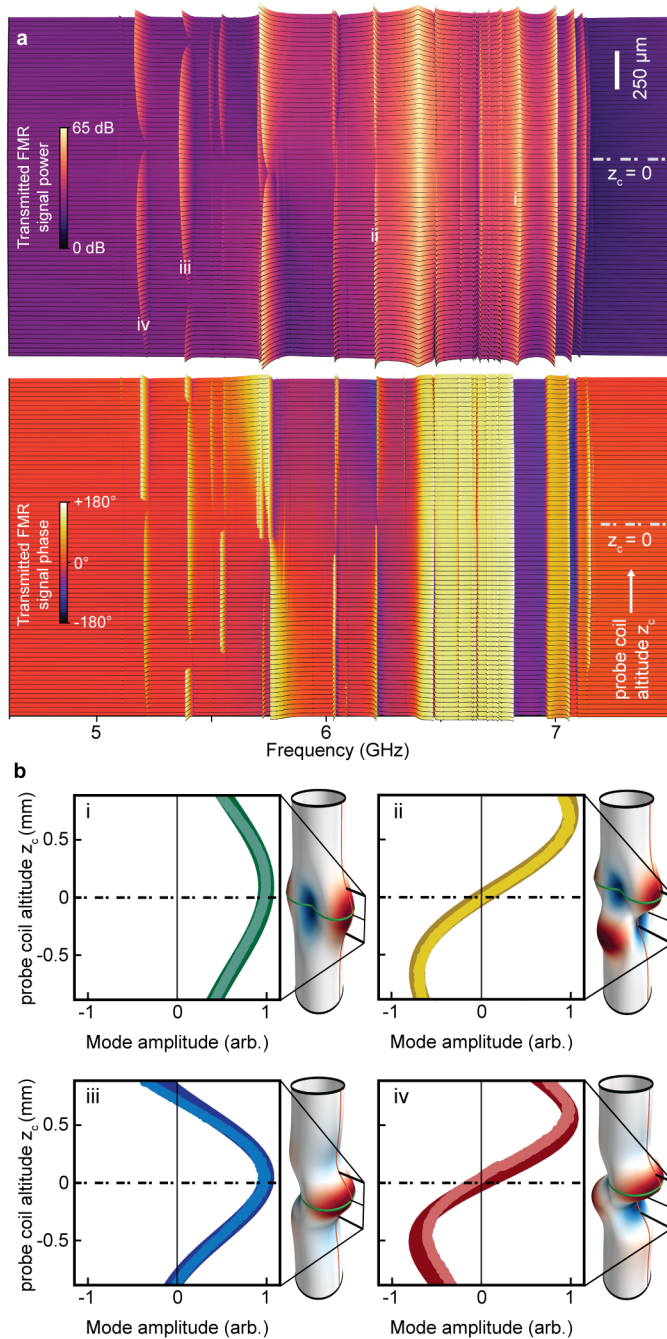


FIG. 4. Altitude dependence of the induced magnetic flux. **a**, Microwave transmission spectra in power and phase as a function of the altitude position z_c of the probe coil. **b**, Extraction of the local response of the modes allowing the reconstruction of their structure along the altitude axis (light-color filled circles), exemplified here for the lower-order families (i) $n - |m| = 0$, (ii) $n - |m| = 1$, (iii) $n - |m| = 2$ and (iv) $n - |m| = 3$. They are illustrated respectively by the modes of mean eigenfrequencies 6.82 GHz, 6.23 GHz, 5.42 GHz and 5.23 GHz (indicated on **a** and on Fig. 2**b** with orange stars), identified as (2, 2, 0), (3, 2, 0), (3, 1, 0) and (4, 1, 0). Note that (i) and (iii) were represented in Fig. 3, respectively labeled (iii) ($m = 2$) and (ii) ($m = 1$). The solid dark lines correspond to the expected flux ($\tilde{r}_c = 2$ mm, $\Delta_y = 0.5$ mm, $\Delta_z = 0.3$ mm) with a coil axis tilt $\xi_z = -6^\circ$. The altitude extent of these plots is depicted as a black rectangle in the insets showing the magnetic flux distribution.

* arnaud.gloppe@qc.rcast.u-tokyo.ac.jp

- [1] H. J. Kimble, *Nature* **453**, 1023 (2008).
- [2] X. Zhang, C.-L. Zou, L. Jiang, and H. Tang, *Science Advances* **2** (2016).
- [3] Y. Tabuchi, S. Ishino, A. Noguchi, T. Ishikawa, R. Yamazaki, K. Usami, and Y. Nakamura, *Science* **349**, 405 (2015).
- [4] R. Hisatomi, A. Osada, Y. Tabuchi, T. Ishikawa, A. Noguchi, R. Yamazaki, K. Usami, and Y. Nakamura, *Phys. Rev. B* **93**, 174427 (2016).
- [5] L. R. Walker, *Phys. Rev.* **105**, 390 (1957).
- [6] L. R. Walker, *Journal of Applied Physics* **29**, 318 (1958).
- [7] P. C. Fletcher and R. O. Bell, *Journal of Applied Physics* **30**, 687 (1959).
- [8] J. F. Dillon, *Journal of Applied Physics* **31**, 1605 (1960).
- [9] A. Osada, R. Hisatomi, A. Noguchi, Y. Tabuchi, R. Yamazaki, K. Usami, M. Sadgrove, R. Yalla, M. Nomura, and Y. Nakamura, *Phys. Rev. Lett.* **116**, 223601 (2016).
- [10] J. A. Haigh, A. Nunnenkamp, A. J. Ramsay, and A. J. Ferguson, *Phys. Rev. Lett.* **117**, 133602 (2016).
- [11] X. Zhang, N. Zhu, C.-L. Zou, and H. X. Tang, *Phys. Rev. Lett.* **117**, 123605 (2016).
- [12] S. Viola-Kusminskiy, H. X. Tang, and F. Marquardt, *Phys. Rev. A* **94**, 033821 (2016).
- [13] S. Sharma, Y. M. Blanter, and G. E. W. Bauer, *Phys. Rev. B* **96**, 094412 (2017).
- [14] A. Osada, A. Gloppe, R. Hisatomi, A. Noguchi, R. Yamazaki, M. Nomura, Y. Nakamura, and K. Usami, *Phys. Rev. Lett.* **120**, 133602 (2018).
- [15] P. Lodahl, S. Mahmoodian, S. Stobbe, A. Rauschenbeutel, P. Schneeweiss, J. Volz, H. Pichler, and P. Zoller, *Nature* **541**, 473 (2017).
- [16] S. Barzanjeh, S. Guha, C. Weedbrook, D. Vitali, J. Shapiro, and S. Pirandola, *Phys. Rev. Lett.* **114**, 080503 (2015).
- [17] J. A. Haigh, N. J. Lambert, S. Sharma, Y. M. Blanter, G. E. W. Bauer, and A. J. Ramsay, *Phys. Rev. B* **97**, 214423 (2018).
- [18] P. Fletcher, I. H. Solt, and R. Bell, *Phys. Rev.* **114**, 739 (1959).
- [19] I. H. J. Solt and P. C. Fletcher, *Journal of Applied Physics* **31**, S100 (1960).
- [20] P. C. Fletcher and I. H. J. Solt, *Journal of Applied Physics* **30**, S181 (1959).
- [21] S. Klingler, H. Maier-Flaig, C. Dubs, O. Surzhenko, R. Gross, H. Huebl, S. T. B. Goennenwein, and M. Weiler, *Applied Physics Letters* **110**, 092409 (2017).
- [22] N. Kostylev, M. Goryachev, and M. E. Tobar, *Appl. Phys. Lett.* **108**, 062402 (2016).
- [23] S. Sharma, Y. Blanter, and G. Bauer, *Phys. Rev. Lett.* **121**, 087205 (2018).
- [24] H. Stoll, A. Puzic, B. van Waeyenberge, P. Fischer, J. Raabe, M. Bues, T. Haug, R. Höllinger, C. Back, D. Weiss, and G. Denbeaux, *Appl. Phys. Lett.* **84**, 3328 (2004).
- [25] S. Tamaru, J. A. Bain, R. J. M. van de Veerdonk, T. M. Crawford, M. Covington, and M. H. Kryder, *Journal of Applied Physics* **91**, 8034 (2002).
- [26] T. An, K. Yamaguchi, K. Uchida, and E. Saitoh, *Appl. Phys. Lett.* **103**, 052410 (2013).

- [27] S. Lee, C. P. Vlahacos, B. J. Feenstra, A. Schwartz, D. E. Steinhauer, F. C. Wellstood, and S. M. Anlage, *Appl. Phys. Lett.* **77**, 4404 (2000).
- [28] I. Lee, Y. Obukhov, G. Xiang, A. Hauser, F. Yang, P. Banerjee, D. V. Pelekhan, and P. C. Hammel, *Nature* **466**, 845 (2010).
- [29] D. A. Gurnett and B. J. O'Brien, *Journal of Geophysical Research* **69**, 65 (1964).
- [30] J. E. P. Connerney *et al.*, *Science* **356**, 826 (2017).
- [31] P. C. Lauterbur, *Nature* **242**, 190 (1973).
- [32] See Supplementary Information.
- [33] A. Gurevich and G. A. Melkov, *Magnetization Oscillations and Waves* (CRC Press, 1996).

Methods

Spin-wave modes calculations

The spin-wave modes in Fig. 1a are plotted at time $t = 0.2 \times 2\pi/\Omega_k$, with a saturation magnetization $M_s = 194 \text{ mT}/\mu_0$, a static magnetic field $H_{\text{DC}} = 315 \text{ mT}/\mu_0$ and a gyromagnetic ratio $\gamma/2\pi = 28 \text{ GHz}/\text{T}$. The resonance frequency $\Omega_k/2\pi$ of a given spin-wave mode is numerically determined by solving the resonance equation (S19) in these conditions [32], a requirement to define properly the oblate spheroidal coordinate system in which the internal magnetic potential has explicit solutions, computed for each colatitude θ . Once interpolated on a regular Cartesian grid, the internal magnetic potential is numerically differentiated to obtain the internal magnetic field. The transverse magnetization \mathbf{M}_n^m is obtained by linear combination of the internal magnetic field components with oblate factors, as functions of H_{DC} and M_s [7]. The stray field is numerically evaluated from the external magnetic potential ψ_n^m . The internal and external fields for $(3, 3, 0)$ are joined to plot the total transverse magnetic induction field \mathbf{B}_3^3 in Figure 1b, slightly out of resonance for a better visualization.

Experimental setup

The sample is attached to the end of a Al_2O_3 rod going through the upper permanent ring magnet, on a three-axis linear actuator. The centering of the sample with respect to the rotation stage axis is performed with the help of a CMOS camera, placed on the rotation stage to move jointly with the probe coil (see [32] for a detailed view on the experimental setup). A solenoid is wound around the magnetic circuit to tune the static

field ($\sim \pm 14 \text{ mT}$). The motorized rotation stage is an *Optosigma HST-120YAW* (0.1° position accuracy). The linear motors are composed by *Optosigma TAMM40-10C* (10 mm travel range, $6 \mu\text{m}$ position accuracy) and *HPS60-20X-M5* (20 mm travel range, $15 \mu\text{m}$ position accuracy). The probe coil plane tilt is corrected with a small manual rotation stage *Optosigma KSP-256*.

Probe coil

The coil parameters Δ_y , Δ_z and \tilde{r}_c are chosen carefully to ensure proper imaging. The detection distance \tilde{r}_c should be short to maximize the acquired signal ($\phi_n^m \propto 1/\tilde{r}_c^{m+2}$) while insuring that $\Delta_y/\tilde{r}_c \ll 1$ and $\Delta_z/\tilde{r}_c \ll 1$. The lateral semi-extension Δ_y while small compared to \tilde{r}_c , should be maximized ($\phi_n^m \propto \Delta_y$). The value of Δ_z should be small enough to guarantee the structure measured can be safely related to $n - |m|$. The choice of $\Delta_z = 0.3 \text{ mm}$ for $\tilde{r}_c = 2 \text{ mm}$ insures the safe detection of spin-wave modes with $n - |m|$ up to 11. The distance \tilde{r}_c may be slightly tuned to maximize the detection of a particular azimuth family (see [32] for details).

Data acquisition

In the magnetostatic approximation [6], the spin-wave modes are expected on a frequency range of $\gamma\mu_0 M_s/4\pi \sim 2.6 \text{ GHz}$. The information on all the observable spin-wave modes is obtained with a high resolution by acquiring the spectra by pieces, for a total range of 2.89 GHz and more than 65,000 points by spectrum (microwave excitation power: 0 dBm). At fixed altitude, we record spectra at 101 different probe coil azimuthal positions on a 158° range. The accessible angular range is limited by the presence of the magnetic circuit and pump coil. At fixed azimuth, we record spectra at 297 different probe altitudes on a 2.2 mm extent across the equatorial plane of the sphere. A residual background from the direct coupling between the coils and the parasitic response of close-by elements subsists with typical linewidths ($> 1 \text{ GHz}$) much larger than those of the spin-wave modes ($< 10 \text{ MHz}$) and could be then conscientiously dismissed. A set of measurement at a given coil position lasts for 4 min with a resolution bandwidth of 10 kHz, resulting in a total measurement time of 6 h along the azimuth (Figure 3) and 22 h along the altitude (Figure 4).